



# Origin of ultrahigh-performance barium titanate-based piezoelectrics: Stannum-induced intrinsic and extrinsic contributions

Received: 20 June 2024

Accepted: 23 August 2024

Published online: 04 September 2024

Bo Wu<sup>1,2,8</sup>, Huijing Zheng<sup>1,8</sup>, Yan-Qi Wu<sup>2,8</sup>, Zhicheng Huang<sup>3,8</sup>,  
Hao-Cheng Thong<sup>2</sup>, Hong Tao<sup>1</sup>, Jian Ma<sup>1</sup>, Chunlin Zhao<sup>1,4</sup>✉, Ze Xu<sup>1,2</sup>,  
Yi-Xuan Liu<sup>2</sup>, Zhipeng Xing<sup>2</sup>, Naixin Liang<sup>3</sup>, Fang-Zhou Yao<sup>5</sup>✉, Chao-Feng Wu<sup>6</sup>,  
Ke Wang<sup>1,2</sup> & Bing Han<sup>1,2</sup>✉

Check for updates

Despite the pivotal role of stannum doping in achieving ultrahigh piezoelectric performance in barium titanate-based ceramics, the fundamental mechanisms underlying this enhancement remain elusive. Here, we introduce a single variable nonstoichiometric stannum strategy in lead-free barium titanate-based ceramics with giant piezoelectricity, revealing that stannum doping contributes intrinsically and extrinsically to enhance piezoelectricity. Density functional theory calculations elucidate the intrinsic enhancement of polarization arising from lattice distortion and increased space for titanium-oxygen bonds induced by optimal stannum doping, which is corroborated by Rayleigh analysis. A phase transition from ferroelectric multiphase coexistence to paraelectric phase is observed, alongside a rapid miniaturized and eventually disappeared domains with increasing stannum doping. This evolution in phase structure and domain configuration induces a nearly vanishing polarization anisotropy and low domain wall energy, facilitating easy polarization rotation and domain wall motion, thereby significantly contributing to the extrinsic piezoelectric response. Consequently, the origins of ultrahigh performance can be attributed to the synergistic effect of stannum-induced intrinsic and extrinsic contributions in barium titanate-based ceramics. This study provides fundamental insights into the role of doping elements and offers guidance for the design of high-performance piezoelectrics.

Perovskite ferroelectrics, renowned for converting mechanical energy into electrical energy and vice versa, serve as foundational materials across various applications, including military actuators, electronic sensors, and medical ultrasonic transducers<sup>1–9</sup>. Nowadays, the global

market for piezoelectric and ferroelectric devices is projected to expand into a multi-billion-dollar industry, with an annual growth rate of 13.2%<sup>6</sup>. High-performance lead zirconate titanate [Pb(Zr, Ti)O<sub>3</sub>, PZT]-based piezoelectric ceramics have been employed extensively in

<sup>1</sup>Sichuan Zoige Alpine Wetland Ecosystem National Observation and Research Station, Sichuan Province Key Laboratory of Information Materials, Southwest Minzu University, Chengdu, P. R. China. <sup>2</sup>State Key Laboratory of New Ceramics and Fine Processing, School of Materials Science and Engineering, Tsinghua University, Beijing, P. R. China. <sup>3</sup>Department of Thoracic Surgery, Peking Union Medical College Hospital, Chinese Academy of Medical Sciences and Peking Union Medical College, Beijing, China. <sup>4</sup>College of Materials Science and Engineering, Fuzhou University, Fuzhou, P. R. China. <sup>5</sup>Research Center for Advanced Functional Ceramics, Wuzhen Laboratory, Jiaxing, P. R. China. <sup>6</sup>Center of Advanced Ceramic Materials and Devices, Yangtze Delta Region Institute of Tsinghua University, Zhejiang, China. <sup>7</sup>Department of Orthodontics, Peking University School and Hospital of Stomatology, Beijing, P. R. China. <sup>8</sup>These authors contributed equally: Bo Wu, Huijing Zheng, Yan-Qi Wu, Zhicheng Huang. ✉e-mail: zhaochunlin@fzu.edu.cn; yaofangzhou@xjtu.edu.cn; kqbinghan@bjmu.edu.cn

piezoelectric devices due to their superior piezoelectric coefficients and high Curie temperature, thereby dominating the piezoelectric ceramics market<sup>10</sup>. However, the societal ramifications of lead pollution, such as cancer, fetal malformations, and food safety concerns, are becoming increasingly severe<sup>10–12</sup>. In pursuit of sustainable development, legislation and regulations have been enacted or strengthened globally in response to escalating ecological and environmental concerns, thereby directing significant attention toward the development of lead-free piezoelectric materials<sup>3–5,11</sup>.

As the earliest discovered perovskite-type lead-free ferroelectrics, barium titanate ( $\text{BaTiO}_3$ , BT)-based ceramics have been extensively studied for their remarkable properties, particularly their piezoelectric performance<sup>10,12–21</sup>. To meet specific device requirements, chemical modification is the most commonly employed method to tailor the electrical properties of BT-based ceramics<sup>12</sup>. The hybridization between B-site atoms and oxygen atoms is fundamentally responsible for the ferroelectricity observed in BT-based ceramics<sup>22</sup>. The associated physical characteristics, such as lattice distortion, domain configuration, and phase boundary, can be modulated through chemical substitution or doping<sup>12</sup>. For example, high piezoelectricity can be achieved through ions doping to shift the phase-transition temperature and form the multiphase boundary. The increase in dielectric permittivity, hierarchical domain structure, and more directions of polarization rotation after chemical substitution or doping are identified as the origins of enhanced piezoelectricity near the phase boundary where the polarization vectors can be easily

rotated due to the low energy barrier<sup>3,9,12</sup>. This substitution typically involves replacing cations at either the A or B sites within the BT-based ceramics. Low-valence ions are commonly incorporated into the A site, displacing  $\text{Ba}^{2+}$  ions, while high-valence ions are generally introduced into the B site to replace  $\text{Ti}^{4+}$  ions. To achieve desirable piezoelectric properties, isovalent substitution has proven to be the most effective strategy for altering the structural and functional attributes of BT-based ceramics<sup>10,12–21</sup>. The most frequently utilized cations for substitution at the  $\text{Ba}^{2+}$  site are  $\text{Ca}^{2+}$  or  $\text{Sr}^{2+}$ , while valence-stable  $\text{Zr}^{4+}$ ,  $\text{Hf}^{4+}$ , and  $\text{Sn}^{4+}$  cations are preferred for substituting  $\text{Ti}^{4+}$  at the B site due to their comparable ionic valence and radii, as shown in Fig. 1a. The construction of a multiphase boundary has garnered significant attention, as the isovalent substitution of  $\text{Zr}^{4+}$ ,  $\text{Hf}^{4+}$ , and  $\text{Sn}^{4+}$  for  $\text{Ti}^{4+}$  significantly enhances the piezoelectric properties of BT-based ceramics<sup>12</sup>.

BT ceramics undergo three distinct phase transitions—tetragonal-cubic (T-C), orthorhombic-tetragonal (O-T), and rhombohedral-orthorhombic (R-O)—as the temperature decreases from high to low<sup>9</sup>. The introduction of  $\text{Zr}^{4+}$ ,  $\text{Hf}^{4+}$ , and  $\text{Sn}^{4+}$  into the B site of BT shifts the R-O transition temperature ( $T_{\text{R-O}}$ ) and the O-T transition temperature ( $T_{\text{O-T}}$ ) to higher temperatures while simultaneously decreasing the T-C transition temperature ( $T_{\text{C}}$ ), as illustrated in Fig. 1b. The doping of  $\text{Zr}^{4+}$  and  $\text{Hf}^{4+}$  exhibits similar effects on shifting the phase-transition temperatures ( $T_{\text{R-O}}$ ,  $T_{\text{O-T}}$ , and  $T_{\text{C}}$ ) of BT-based ceramics. However, the rate of increase in  $T_{\text{R-O}}$  and  $T_{\text{O-T}}$  induced by  $\text{Sn}^{4+}$  substitution is slower compared to that of  $\text{Zr}^{4+}$  or  $\text{Hf}^{4+}$  substitution,

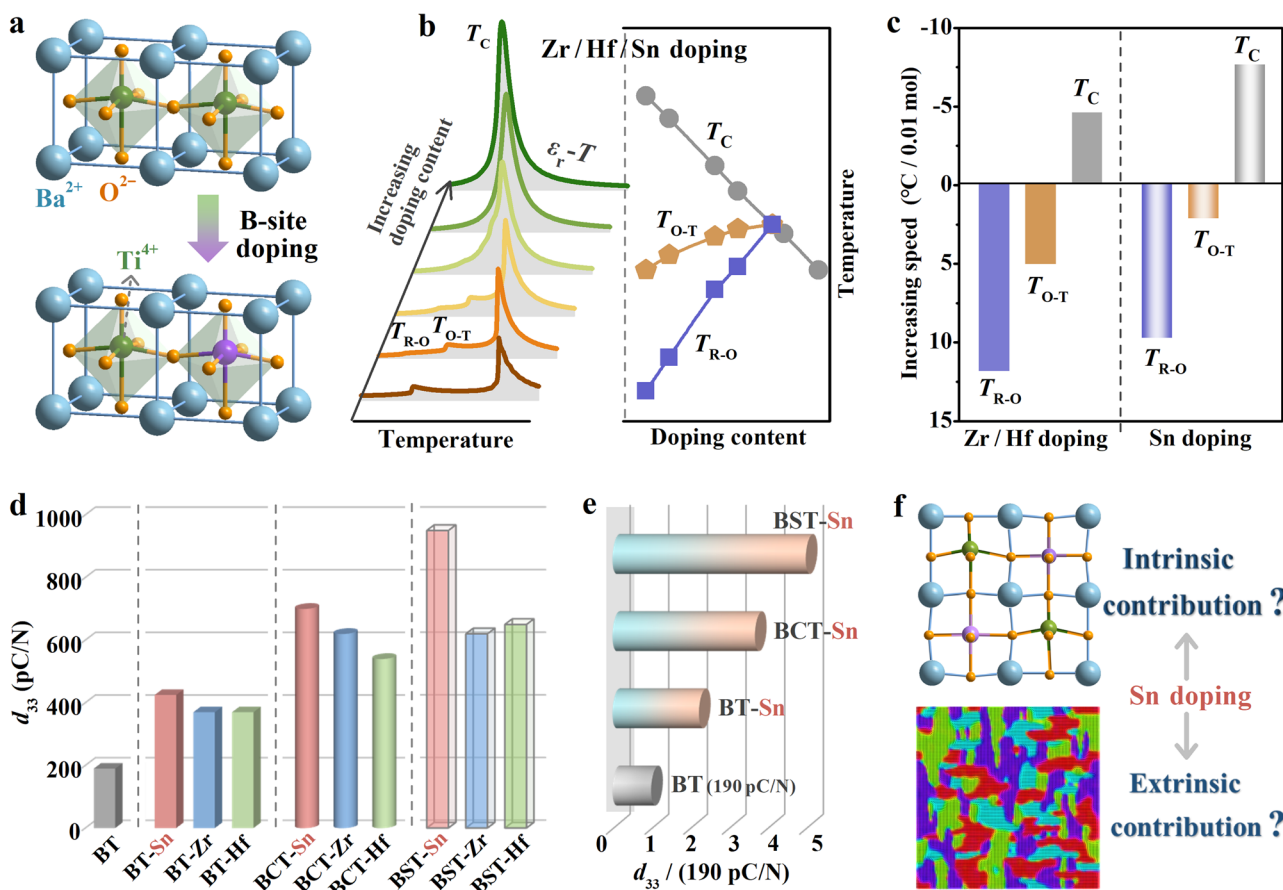


**Fig. 1 | Sn-doped barium titanate (BT)-based piezoelectrics with higher piezoelectric performance.** **a** Schematic of B-site doping in  $\text{ABO}_3$  structure. **b** Relative dielectric permittivity-temperature ( $\epsilon_r$ -T) curves and phase diagram. **c** Increasing speed of phase transition temperatures from rhombohedral to orthorhombic phases ( $T_{\text{R-O}}$ ), from orthorhombic to tetragonal phases ( $T_{\text{O-T}}$ ), and Curie temperature ( $T_{\text{C}}$ ) for B-site  $\text{Zr}^{4+}$ ,  $\text{Hf}^{4+}$ , or  $\text{Sn}^{4+}$  doped BT ceramics<sup>12</sup>. **d** Piezoelectric coefficient ( $d_{33}$ ) of BT and BT-based ceramics with B-site  $\text{Zr}^{4+}$ ,  $\text{Hf}^{4+}$  or  $\text{Sn}^{4+}$  substitution. **e**  $d_{33}/190 \text{ pC/N}$  for BT and BT-based ceramics with B-site  $\text{Sn}^{4+}$  doping. **f** Schematic of contribution on ultrahigh piezoelectric performance for Sn doping in BT-based ceramics.

temperature ( $T_{\text{C}}$ ) for B-site  $\text{Zr}^{4+}$ ,  $\text{Hf}^{4+}$ , or  $\text{Sn}^{4+}$  doped BT ceramics<sup>12</sup>. **d** Piezoelectric coefficient ( $d_{33}$ ) of BT and BT-based ceramics with B-site  $\text{Zr}^{4+}$ ,  $\text{Hf}^{4+}$  or  $\text{Sn}^{4+}$  substitution. **e**  $d_{33}/190 \text{ pC/N}$  for BT and BT-based ceramics with B-site  $\text{Sn}^{4+}$  doping. **f** Schematic of contribution on ultrahigh piezoelectric performance for Sn doping in BT-based ceramics.

whereas the decrease in  $T_C$  is more pronounced with  $\text{Sn}^{4+}$  doping. To quantitatively describe the impact on phase boundary shifts, the average rates of change for  $T_{\text{R-O}}$ ,  $T_{\text{O-T}}$  and  $T_C$  with  $\text{Zr}^{4+}$ ,  $\text{Hf}^{4+}$ , or  $\text{Sn}^{4+}$  substitution are plotted in Fig. 1c. Specifically,  $T_{\text{R-O}}$  increases by approximately  $11.8^\circ\text{C}$  per mol% and  $T_{\text{O-T}}$  by around  $5.0^\circ\text{C}$  per mol%, while  $T_C$  decreases by approximately  $4.6^\circ\text{C}$  per mol% with the moderate substitution of  $\text{Zr}^{4+}$  or  $\text{Hf}^{4+}$  at the B site. Interestingly,  $\text{Sn}^{4+}$  substitution at the B site results in the improvement by approximately  $9.7^\circ\text{C}$  per mol% for  $T_{\text{R-O}}$  and  $2.1^\circ\text{C}$  per mol% for  $T_{\text{O-T}}$ , and the descent by  $7.7^\circ\text{C}$  per mol% for  $T_C$  in BT ceramics<sup>12</sup>. Based on the effects of  $\text{Zr}^{4+}$ ,  $\text{Hf}^{4+}$ , and  $\text{Sn}^{4+}$  substitutions at the B site, an ideal multiphase boundary can be successfully constructed to improve piezoelectric properties<sup>12,18</sup>. Figure 1d presents the piezoelectric properties of various BT-based ceramics with  $\text{Zr}^{4+}$ ,  $\text{Hf}^{4+}$ , or  $\text{Sn}^{4+}$  substitution, which are comparable to those of traditional lead-based piezoelectric ceramics. All the BT-based ceramics with chemical substitution exhibit a higher piezoelectric property than that of pure BT ceramics, particularly for the ceramics with co-substitution at A/B sites (A site:  $\text{Ca}^{2+}$ ,  $\text{Sr}^{2+}$ ; B site:  $\text{Zr}^{4+}$ ,  $\text{Hf}^{4+}$ , and  $\text{Sn}^{4+}$ )<sup>12,15-21</sup>. Although  $\text{Zr}^{4+}$ ,  $\text{Hf}^{4+}$ , and  $\text{Sn}^{4+}$  substitutions enhance the piezoelectric properties,  $\text{Sn}^{4+}$  is the most effective dopant at the B site in BT-based ceramics, as shown in Fig. 1e. Nevertheless, the origin of this ultrahigh performance in Sn-doped BT-based piezoelectrics remains unclear. Therefore, understanding how Sn dopants contribute to enhancing piezoelectric properties intrinsically and extrinsically remains a critical area for further research (See Fig. 1f).

To this end, a kind of BT-based composition with A/B site co-substitution (A site:  $\text{Sr}^{2+}$ ; B site:  $\text{Sn}^{4+}$ ) locates at the multiphase boundary, achieving a high piezoelectricity  $d_{33}$  up to  $850 \text{ pC N}^{-1}$ . To reveal the contribution of Sn dopant on ultrahigh-performance BT-based piezoelectrics, a nonstoichiometric strategy with a single variable was implemented in  $\text{Ba}_{0.86}\text{Sr}_{0.14}\text{Ti}_{0.92}\text{Sn}_{0.08+x}$  ( $x = -0.02$ , 0, and 0.02; abbreviated as BSTS<sub>0.08+x</sub>). Our study integrates high-resolution transmission electron microscopy (TEM), piezoresponse force microscopy (PFM), density functional theory (DFT), and Rayleigh analysis to examine the contribution to piezoelectric performance in three pre-selected compositions with varying Sn content. Here, the extrinsic contribution mainly results from the domain switching and domain wall motion, and the contribution by phase boundary. The intrinsic piezoelectric response related to the lattice distortion contributes to the intrinsic contribution<sup>9</sup>. The increased intrinsic contribution arises from the enhancement of polarization, resulting from lattice distortions and increased space for Ti-O bonds in the ceramics with a small amount of Sn doping. The domain becomes quite small as the phase transitions from O-T to R-O-T, facilitating the piezoelectricity due to the easy domain wall motion under an external field. Benefiting from the synergy of intrinsic and extrinsic contributions induced by Sn doping, an ultrahigh  $d_{33}$  is obtained. This work offers fundamental insights for designing high-performance piezoelectric materials through chemical modification.

## Results

### Structure and nonstoichiometric characterization

In view of the ionic radius difference between  $\text{Ti}^{4+}$  ( $0.605 \text{ \AA}$ , CN = 6) and  $\text{Sn}^{4+}$  ( $0.69 \text{ \AA}$ , CN = 6), it is essential to analyze the stability of the perovskite structure after doping. The stability can be assessed using the tolerance factor ( $\tau$ ), defined by the following formula<sup>23,24</sup>:

$$\tau = \frac{R_A + R_B}{\sqrt{2}(R_B + R_O)} \quad (1)$$

where  $\tau$  is the tolerance factor, and  $R_A$ ,  $R_B$ , and  $R_O$  are the ionic radii of the A-site, B-site, and oxygen ions in the  $\text{ABO}_3$  perovskite structure, respectively. For a complex perovskite, the values for  $R_A$  and  $R_B$  are

normalized by the atomic ratio. The average ionic radius at the A site and B site can be calculated using the following equations:

$$R_A = 0.86R_{\text{Ba}^{2+}} + 0.14R_{\text{Sr}^{2+}} \quad (2)$$

$$R_B = 0.92R_{\text{Ti}^{4+}} + (0.08 + x)R_{\text{Sn}^{4+}} \quad (3)$$

where the ionic radius of  $\text{Ba}^{2+}$  and  $\text{Sr}^{2+}$  at A site (CN = 12) are  $1.61 \text{ \AA}$  and  $1.44 \text{ \AA}$ , respectively. The radius of  $\text{Ti}^{4+}$  and  $\text{Sn}^{4+}$  at B site (CN = 6) are  $0.605 \text{ \AA}$  and  $0.69 \text{ \AA}$ , and the radii of  $\text{O}^{2-}$  is  $1.40 \text{ \AA}$ . Notably, all  $\tau$  remains approximately 1 for all compositions ( $\tau_{-0.02}$ : 1.057,  $\tau_{0.00}$ : 1.0496,  $\tau_{0.02}$ : 1.042), indicating that the BSTS<sub>0.08+x</sub> ceramics exhibit the high stability of  $\text{ABO}_3$  structure<sup>23,24</sup>.

A typical perovskite structure is achieved without any secondary phases in BSTS<sub>0.08+x</sub> ceramics (See Figs. S1 and S2). Figure 2a illustrates the XRD patterns of BSTS<sub>0.08+x</sub> ceramics. The characteristic XRD peak positions shift towards lower angles with increasing  $\text{Sn}^{4+}$  concentration in the range of  $-0.02 \leq x \leq 0.02$ , indicating lattice expansion due to  $\text{Sn}^{4+}$  incorporation. The minimal lattice parameters observed at  $x = -0.02$  can be attributed to the formation of B-site vacancies caused by B-site deficiency<sup>25</sup>. Conversely, the expanded lattice parameters are primarily due to the substitution of smaller-radius  $\text{Ti}^{4+}$  ions with larger-radius  $\text{Sn}^{4+}$  ions at B site<sup>26</sup>. The enlarged Raman spectra around  $515 \text{ cm}^{-1}$  are also presented in Fig. 2a, featuring two peaks corresponding to the  $E$  and  $A_1$  modes. Both  $E$  and  $A_1$  peaks shift to lower wavenumbers regardless of the deficiency or excess of  $\text{Sn}^{4+}$  ions at B site, which can be explained by the weakening of the B-O bond in the ceramics<sup>26-28</sup>. A shift to higher wavenumbers in a Raman mode indicates a stronger chemical bond, while a shift to lower wavenumbers signifies a weaker bond. Consequently, the observed attenuation of the wavenumber at  $x = -0.02$  can be attributed to the formation of vacancies at B site. Furthermore, the downshift in the spectra results from the weakening of the B-O bond when  $\text{Sn}^{4+}$  substitutes for  $\text{Ti}^{4+}$ , due to their differing electronegativities (Sn: 1.96, Ti: 2.04). Additionally, the disparity in ionic radii between  $\text{Sn}^{4+}$  and  $\text{Ti}^{4+}$  induces lattice distortion in the ceramics, further contributing to the weakening of the B-O bond. Thus, the observed shifts of the  $E$  and  $A_1$  peaks to lower wavenumbers corroborate the hypothesis that an excess of  $\text{Sn}^{4+}$  replaces  $\text{Ti}^{4+}$  ( $x = 0.02$ ).

To further elucidate the impact of excess  $\text{Sn}^{4+}$  on the structure, XPS patterns of  $\text{Ti} 2p$  and  $\text{Sn} 3d$  are presented in Fig. 2b. XPS spectra are extensively employed to provide quantitative information on the concentration of specific atoms<sup>29-31</sup>. By calculating the relative content based on the peak area ratio, the proportions of  $\text{Ti}^{4+}$  and  $\text{Sn}^{4+}$  ions can be determined<sup>32,33</sup>. Using  $x = 0$  as the normalization standard, the content ratio of  $\text{Ti}^{4+}$  and  $\text{Sn}^{4+}$  are depicted in Fig. 2c. Notably, the results illustrate that the  $\text{Ti}^{4+}$  content decreases while the  $\text{Sn}^{4+}$  content increases from  $x = -0.02$  to  $x = 0.02$ , thereby corroborating the results conforming to the designed chemical formula. The stoichiometric ratio of Ti and Sn elements is of critical importance for elucidating the relationship between structure and property, which is further analyzed using an Electron Probe Micro-Analyzer (EPMA)<sup>34</sup>. The backscattered electron image (BEI) presents a dense structure in polished samples (see Fig. S3a). Figure 2d reveals no elemental segregation in ceramics with  $x \leq 0$ . However, the Ti element aggregation is observed in ceramics with  $x > 0$ , identifiable by the significant color contrast in the elemental mapping of Ti and Sn. The atomic percentage of the four elements (Ba, Sr, Ti, Sn) is presented in Fig. 2e and Table S1. The discrepancies between theoretical and experimental results are all within 1%, indicating excellent agreement with the stoichiometric composition of BSTS<sub>0.08+x</sub> ceramics, particularly for Ti and Sn. Additionally, BSTS<sub>0.08+x</sub> ceramics show a large but similar average grain size (see Fig. S3b and Table S1), thus the grain size effect on piezoelectric property of these ceramics is insignificant.

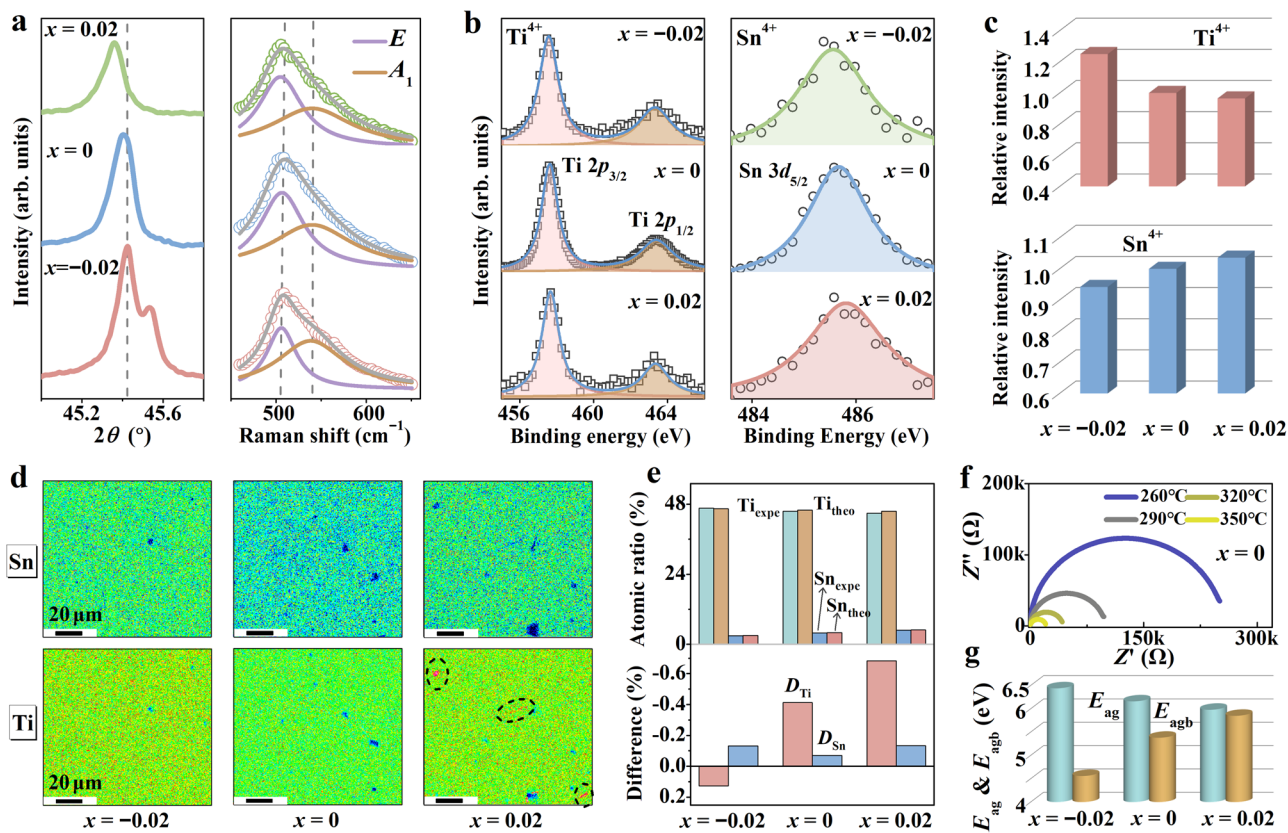


**Fig. 2 | Phase structure and elements characteristics of nonstoichiometric Sn-doped BT.** **a** X-ray diffraction (XRD) patterns and Raman spectra. **b** X-ray photoelectron spectroscopy (XPS) spectra of Ti and Sn. **c** Intensity ratio of Ti and Sn. **d** Electron probe microanalyzer (EPMA) elements mapping of Ti and Sn. **e** Statistical

atomic percentage of the experimental (expe) and theoretical (theo) results, and the difference ( $D$ ) for Ti and Sn. **f** Impedance spectra, and **g** the activation energy of grain ( $E_{ag}$ ) and grain boundary ( $E_{agb}$ ) for  $BSTS_{0.08+x}$  ceramics.

To further elucidate the impact of nonstoichiometry on conductivity mechanisms, impedance spectroscopy was employed. The complex impedance spectra are plotted in Fig. 2f, S4a and S4b. The impedance response is bifurcated into two components: the high-frequency grain response and the low-frequency grain boundary response, attributable to the distinct relaxation times of grain and grain boundary<sup>35,36</sup>. The radius of the semicircles decreases with increasing temperature, which is indicative of charge carrier accumulation near the grain boundaries, thereby reducing resistivity. For a quantitative analysis of the contributions from the grain and grain boundary, the  $Z''-Z'$  curves were fitted using an equivalent circuit model (See Fig. S4c). The activation energy ( $E_a$ ) was estimated using the following equation:

$$\sigma_b = \sigma_0 \exp\left(\frac{-E_a}{kT}\right) \quad (4)$$

where  $\sigma_0$  is the temperature-independent conductivity,  $k$  is the Boltzmann constant, and  $T$  is the absolute temperature. The activation energy for the grain ( $E_{ag}$ ) and grain boundary ( $E_{agb}$ ) can be obtained according to the equation, as is shown in Fig. 2g. It is documented that the  $E_a$  of A-site cations, B-site cations, and oxygen vacancies are approximately 12 eV, 4 eV, and less than 2 eV, respectively<sup>32,37,38</sup>. The calculated  $E_{ag}$  (6.36–6.43 eV) and  $E_{agb}$  values (4.09–6.029 eV) closely align with the  $E_a$  of B-site cations, corroborating the substitution of  $Ti^{4+}$  with  $Sn^{4+}$  at B site. The reduced  $E_{ag}$  is intimately connected to defects arising from the nonstoichiometric effect. A higher  $E_{ag}$  at  $x = -0.02$  is due to defects restricting the migration of free charge carriers within the grain. Additionally, the larger  $E_{agb}$  can be attributed to the accumulation of  $Ti^{4+}$  at the grain boundary, replaced by the excess

$Sn^{4+}$  in the ceramics with  $x = 0.02$ .  $Ti^{4+}$  at the grain boundary is less mobile under an electric field, resulting in a higher  $E_{agb}$ . The presence of defects or elements enrichment is not conducive to obtaining high piezoelectricity since they may impede the polarization rotation and domain wall motion<sup>33</sup>.

#### Macro-performance and extrinsic contribution

As discussed above,  $Sn^{4+}$  doping can elevate the  $T_{R-O}$  and  $T_{O-T}$  while concurrently lowering the  $T_C$ . The nonstoichiometric effect of  $Sn^{4+}$  plays a pivotal role in phase engineering within these ceramics. Figure 3a illustrates the  $\epsilon_r-T$  curves of  $BSTS_{0.08+x}$  ceramics. In the ceramics with  $x \leq 0$ , three distinct dielectric peaks are evident, corresponding to the  $T_C$ ,  $T_{R-O}$ , and  $T_{O-T}$  as the temperature decreases. Conversely, a single dielectric anomalous peak ( $T_C$ ) is observed in the ceramics with  $x > 0$ . The phase transition temperatures for  $BSTS_{0.08+x}$  ceramics can be extracted from the  $\epsilon_r-T$  curves (See Table S2). It indicates that a progression phase transition from O-T to a R-O-T phases coexistence, and ultimately to the C phase. The multiphase coexistence can contribute to high piezoelectric property, particularly for the R-O-T phase coexistence<sup>3,9,12</sup>. To further confirm the evolution of the phase structure, Rietveld refinement was conducted using R ( $R3m$ ), O ( $4mm2$ ), T ( $P4mm$ ), and C ( $Pm3m$ ) crystal symmetries (see Fig. S5). The refinement results exhibit high reliability, as evidenced by the low  $Sig$  (1.27–1.54) and  $R_{wp}$  (6.51–7.71%), with the corresponding structural parameters showing in Table S3. These results corroborate the transformation of phase structure in the ceramic. Additionally, an increase in cell volume is observed in the ceramics with higher Sn content, consistent with the low-angle shift in the XRD patterns. This phenomenon is attributed to the substitution of  $Ti^{4+}$  by  $Sn^{4+}$  at B site.

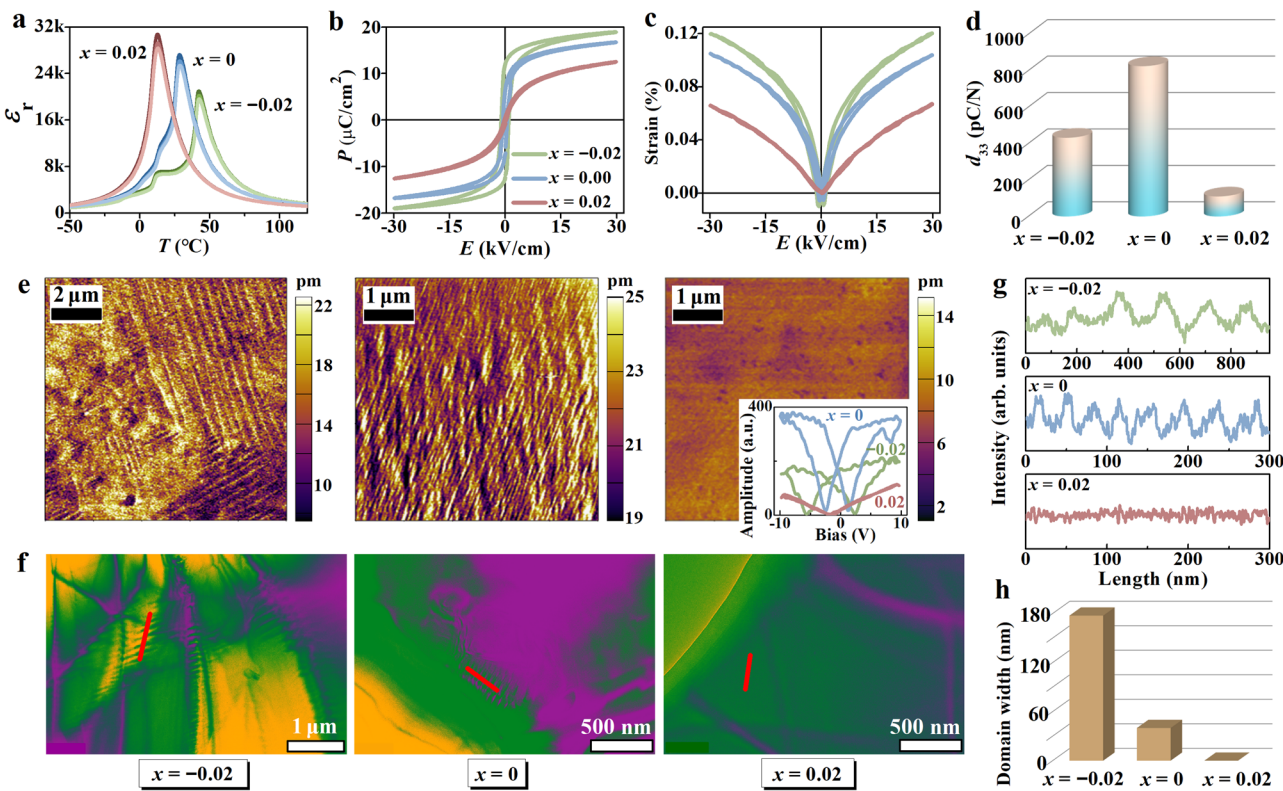


**Fig. 3 | Macroscopic electrical properties and domain structure of non-stoichiometric Sn-doped BT.** **a**, Relative dielectric permittivity-temperature ( $\epsilon_r$ -T) curves; **b**, polarization-electric field ( $P$ -E) loops; **c**, strain-electric field ( $S$ -E) curves; **d**, piezoelectric coefficient ( $d_{33}$ ); **e**, piezoresponse force microscopy (PFM)

amplitude images; **f**, transmission electron microscopy (TEM) images; **g**, statistics of domain width of representative domains marked in TEM images; **h**, domain width of BSTS<sub>0.08+x</sub> ceramics.

Figure 3b, c depicts the  $P$ -E and  $S$ -E loops of the ceramics, measured at 1 Hz and 30 kV/cm. The typical hysteresis loops at  $x \leq 0$  indicate that the ceramics exhibit ferroelectric behavior. Conversely, the ceramics with  $x > 0$  display slender  $P$ -E and  $S$ -E loops, characteristic of a paraelectric phase. The shape of the  $P$ -E and  $S$ -E loops can be further quantified by the squareness ratio ( $R_{sq}$ ) asymmetry ( $\gamma_s$ ), calculated as follows<sup>39,40</sup>:

$$R_{sq} = \frac{P_r}{P_s} + \frac{P_{1.1E_c}}{P_r} \quad (5)$$

$$\gamma_s = \frac{\Delta S^+ - \Delta S^-}{\Delta S^+ + \Delta S^-} \quad (6)$$

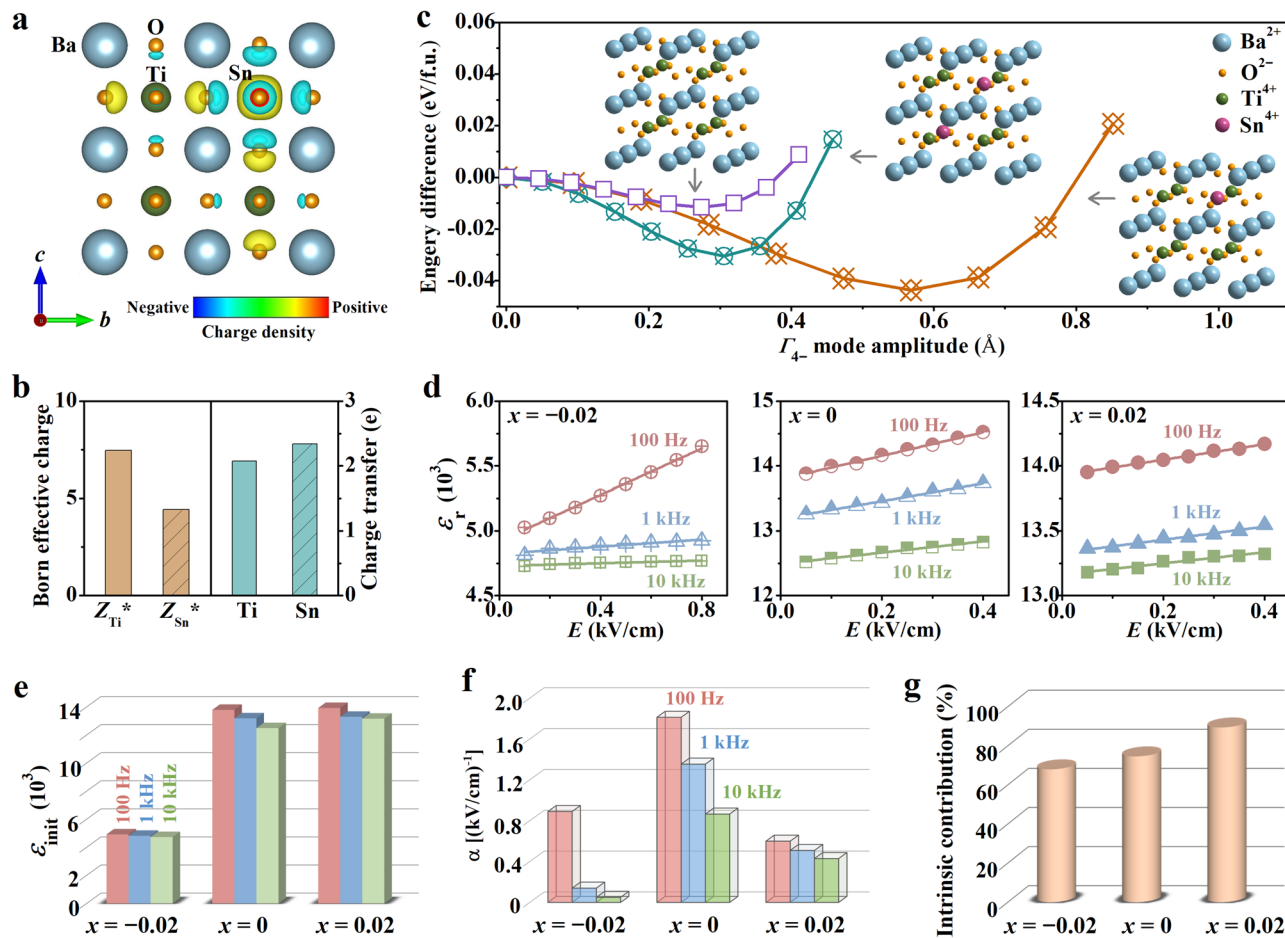
where  $P_r$  is the remanent polarization,  $P_s$  is the saturation polarization,  $P_{1.1E_c}$  is the polarization at 1.1 times the coercive field ( $E_c$ ), and  $\Delta S^-$  and  $\Delta S^+$  are the poling strain of the left and right sides of the  $S$ -E loops, respectively. It is reported that a value of 2 is obtained for perfectly rectangular polarization loops; thus, the decreased  $R_{sq}$  with increasing Sn indicates degraded rectangular  $P$ -E loops<sup>40</sup>. The  $\gamma_s$  remains around 0, suggesting good symmetry of  $S$ -E loops (See Table S4). The related eigenvalues, including  $P_s$ ,  $P_r$ ,  $E_c$ , positive strain ( $S_{pos}$ ), and negative strain ( $S_{neg}$ ), are presented in Table S4. All values decrease with increasing Sn content, which is mainly attributed to the evolution of the phase structure and domain size. Remarkably, the piezoelectric coefficient ( $d_{33}$ ) is significantly enhanced from 432 pC/N to 825 pC/N with increasing Sn from -0.02 to 0.00, and then sharply decreases with excess Sn doping, as shown in Fig. 3d. According to the theoretical relation  $d_{33} \sim \epsilon_r P_r$ , the piezoelectric property is in direct proportion to the product of relative dielectric permittivity and remnant polarization. The variation tendency of  $d_{33}$  is highly consistent with  $\epsilon_r P_r$  (See

Fig. S6), implying that the high dielectric and ferroelectric properties play a crucial role in enhancing the piezoelectric performance<sup>41,42</sup>.

In addition, the domain morphology as well as switching behavior is explored, as shown in Fig. 3e, f. Combining with the amplitude and phase images (Fig. 3e and S7), the miniaturized domain structure with increasing Sn<sup>4+</sup> content is observed (See Fig. 3e), which is also ascribed to the evolution of phase structure. Meanwhile, an optimized piezoelectric response is also gained at  $x=0$  (the insert of Fig. 3e). It is mainly generated by the modified phase content with a lowered energy barrier, which is also the origin of high piezoelectric performance<sup>43</sup>. Based on the PFM and TEM domain images, a stripe ferroelectric domain pattern and obvious non-180° domains are observed in the ceramics with  $x=-0.02$ , indicating strong ferroelectric and strain properties in these ceramics<sup>43</sup>. In contrast, a mottled domain pattern, consisting of numerous nanoscale domains, is observed in the ceramics ( $x=0$ ) along with uniformly distributed elements (See Fig. 3f and S8). This observation suggests the elimination of polarization anisotropy, consistent with high-piezoelectric BT-based ceramics reported elsewhere<sup>13,14</sup>. As Sn content increases, a paraelectric phase devoid of any discernible domains is observed in the ceramics. The evolution of domains is further confirmed by regular intensity fluctuations in microregions marked by dotted lines (See Fig. 3g), with domain size decreasing from 178 nm for  $x=-0.02$  to 37 nm for  $x=0$ , and eventually disappearing (See Fig. 3h). The relationship between piezoelectric property ( $d_{33}$ ) and domain size ( $w_d$ ) follows the formula<sup>44</sup>:

$$d_{33} \approx a + b \times e^{-\frac{w_d}{n}} \quad (7)$$

where  $a$ ,  $b$ , and  $n$  are the constants specific to the piezoelectric material. According to this formula,  $d_{33}$  significantly increases as the



**Fig. 4 | Intrinsic and extrinsic contributions revealed by density functional theory calculation and Rayleigh analysis. a** Charge density distribution; **b** Born effective charge and charge transfer of Ti and Sn in  $\text{BaTiO}_3$  and  $\text{BaSnO}_3$ . **c** Soft phonon mode ( $\Gamma_4$ ) of  $\text{Ba}(\text{Ti}_{1-x}\text{Sn}_x)\text{O}_3$ . **d** Subcoercive measurements of the relative

dielectric permittivity ( $\epsilon_r$ ) for  $\text{BSTS}_{0.08+x}$  ceramics with different frequencies. **e** Initial permittivity ( $\epsilon_{\text{init}}$ ); **f** Rayleigh coefficient ( $\alpha$ ); **g** evolution of intrinsic contribution for  $\text{BSTS}_{0.08+x}$  ceramics.

domain size decreases from 178 nm to 37 nm when composition changes from  $x = -0.02$  to  $x = 0$ , aligning closely with the evolution of  $d_{33}$  observed in the ceramics. Consequently, as Sn content increases, the extrinsic contribution contributed by domain and phase structures increases from  $x = -0.02$  to  $x = 0$  and then decreases at  $x = 0.02$ .

### Intrinsic contribution

It is well-known that the piezoelectric response, similar to the dielectric response under an external electric field, typically exhibits nonlinear and hysteretic characteristics<sup>43</sup>. This behavior arises from the composite nature of the piezoelectric response, which includes both intrinsic and extrinsic contributions. To further elucidate the origin of the intrinsic contribution, the Sn-doped BT ceramics were studied by the density functional theory (DFT) calculations, as depicted in Fig. 4a, b. The Bader charge and charge transfer for Ti are smaller than those for Sn (See Fig. 4a, b, Tables S5–S7). Conversely, the Born effective charge of Ti ( $Z_{\text{Ti}}^* \approx +7.45$ ) is substantially larger than that of Sn ( $Z_{\text{Sn}}^* \approx +4.42$ ), as shown in Fig. 4b. These results suggest that the orbital hybridization between Sn and oxygen atoms is significantly weaker than that between Ti and oxygen atoms. It is well-documented that hybridization between B-site atoms and oxygen atoms mitigates short-range repulsions, facilitating off-center ion displacements and thereby generating dipoles in each unit cell of a conventional ferroelectric<sup>44</sup>. Subsequently, the domain structure is established through the interaction of these dipoles under a long-range Coulomb field. When Sn atoms replace Ti atoms in the unit cells, the dipole formation is

markedly hindered, leading to the disruption of the typical ferroelectric domain structure in BT ceramics. This phenomenon aligns with observations reported elsewhere<sup>44,45</sup>. The lattice volume increases as the concentration of Sn increases due to the larger ionic radius of Sn ions (0.69 Å, CN = 6) substituting the smaller Ti ions (0.605 Å, CN = 6) in BT ceramics (see Tables S8 and S9). This volumetric expansion is corroborated by the XRD patterns. Stress is induced within the matrix by the smaller lattice constants associated with lower Sn concentration in BT ceramics. This stress can expand the polar nanoregions, significantly influencing the ferroelectric properties of the materials<sup>44</sup>. It is reported that the dielectric properties can be greatly strengthened by the mismatch strain due to the different substrates exhibiting different phases in  $\text{BaTiO}_3$  thin films<sup>46</sup>. Notably, increased mismatch strain markedly improves the coercive force and saturation polarization. Here, the stress on the nanoscale domains is three-dimensional, yet the resultant effect is similar. This stress induces an expansion of the unit cells within the nanoscale domains in all three dimensions, creating more space between the Ti atoms and the oxygen octahedra. This increased space facilitates larger off-center displacements, which are directly related to polarization. Consequently, this expansion enhances polarization within the nanoscale domains. To verify the enhanced polarization through theoretical calculations, the soft phonon mode ( $\Gamma_4$ ) corresponding to the origin of ferroelectricity and the paraelectric-ferroelectric phase transition is examined in Fig. 4c. The  $\Gamma_4$  mode initially strengthens in BT ceramics with a small amount of Sn but diminishes with further doping. The enhancement

of  $\Gamma_4$  is attributed to increased polarization induced by lattice distortions and the additional space for Ti-O bonds in BT ceramics with a small amount of Sn. Conversely, more Sn doping disrupts the long-range order, leading to decreased  $\Gamma_4$  and reduced polarization in BT ceramics. As a result, the enhancement of polarization is contributed intrinsically after a small amount of Sn doping, then enhancing the piezoelectric properties.

Given the parallel origins of piezoelectric and dielectric properties, the evolution of intrinsic and extrinsic contributions in dielectric behavior is similarly applicable to piezoelectric performance. To delineate the reversible and irreversible contributions on dielectric activities, Rayleigh analysis was employed. The electric-field dependence of the dielectric permittivity [ $\epsilon(E)$ ] of BSTS<sub>0.08+x</sub> ceramics is illustrated in Fig. 4d, measured under subcoercive conditions in the low-field regime ( $\leq 0.8$  kV/cm), where domain structure and domain wall density remain unchanged. The  $\epsilon(E)$  increases monotonically with applied electric fields at different frequencies (100 Hz, 1000 Hz, and 10000 Hz), consistent with the Rayleigh relationship<sup>13,16,40</sup>:

$$\epsilon(E) = \epsilon_{init} + \alpha E \quad (8)$$

where  $\epsilon(E)$  is the field-dependent permittivity,  $\alpha$  is the Rayleigh coefficient,  $\epsilon_{init}$  is the field-independent initial permittivity, and  $E$  is the applied electric field. Significantly,  $\epsilon_{init}$  reflects the reversible dielectric response, attributable to lattice deformation and reversible domain wall motion, thus is frequency-dependent. Conversely, the irreversible dielectric response is encapsulated by the coefficient  $\alpha E$ . The fitted results align well with the electric-field dependence of dielectric permittivity. The increase in  $\epsilon_{init}$  indicates an enhancement in contributions from reversible domain wall motion and intrinsic ionic response, as shown in Fig. 4e. The coefficient  $\alpha$  initially increases and then decreases with increasing Sn, suggesting that the irreversible domain activity becomes stronger firstly and then attenuated (See Fig. 4f), regardless of the frequency. As frequency increases, both  $\epsilon_{init}$  and  $\alpha$  decrease in the ceramics. The reduction in  $\epsilon_{init}$  may be ascribed to a weakened reversible domain response, while the decline in  $\alpha$  results from deteriorated irreversible domain activity under a higher frequency. Additionally, the intrinsic contributions can be estimated using the following equation:

$$C_{intri} = \frac{\epsilon_{init}}{\epsilon_r} \quad (9)$$

where  $C_{intri}$  represents the proportion of intrinsic contribution. Notably, the increased  $C_{intri}$  indicates that the intrinsic contribution rises with increasing Sn, as shown in Fig. 4g. In addition, the larger proportion of intrinsic contribution makes a major contribution to the  $\epsilon_r$ , as does  $d_{33}$ . Thus, the intrinsic contribution to the piezoelectric property is also enhanced in the ceramics with increasing Sn.

## Discussion

In summary, the origin of the ultrahigh piezoelectric performance has been revealed in Sn-doped BT-based ceramics with the nonstoichiometric Sn strategy. To understand how Sn dopant contributes to enhancing piezoelectric properties, the Sn-induced intrinsic and extrinsic contribution is systematically investigated in BSTS<sub>0.08+x</sub> ceramics. It is found that the common supports from the intrinsic and extrinsic contributions facilitate the ultrahigh piezoelectricity in Sn-doped BT-based ceramics. The intrinsic contribution pertains to the linear piezoelectric effect associated with lattice distortion. The enhancement of polarization arises from lattice distortions and increased space for Ti-O bonds, induced by a small amount of Sn doping, which intrinsically contributes to enhancing the piezoelectric properties. Conversely, the extrinsic contribution reflects the

piezoelectric response resulting from the movement of interfaces within the piezoelectrics, particularly phase boundary and domain wall. With the Sn doping, the evolution of phase structure from O-T to R-O-T phases coexistence and the miniaturized domains result in a nearly vanishing polarization anisotropy and thus low domain wall energy facilitating easy polarization rotation and domain wall motion, which finally leads to strong piezoelectricity. This work provides a fundamental understanding of the role of Sn dopant, offering valuable insights for designing doping processes and developing high-performance piezoelectric materials.

## Methods

### Sample preparation

Ba<sub>0.86</sub>Sr<sub>0.14</sub>Ti<sub>0.92</sub>Sn<sub>0.08+x</sub> ( $x = -0.02, 0$ , and  $0.02$ , abbreviated as BSTS<sub>0.08+x</sub>) ceramics were prepared by conventional solid-state method. Raw materials BaCO<sub>3</sub> (99.0%), SrCO<sub>3</sub> (99.0%), SnO<sub>2</sub> (99.5%), and Ti-O<sub>2</sub> (98.0%) produced by Sinopharm Chemical Reagent Co., Ltd., were weighed and ball milled for 24 hours with both ZrO<sub>2</sub> ball media and alcohol. The powder mixture was calcined at 1200 °C for 2 hours. Subsequently, the powders were pressed into pellets with the addition of 8 wt% polyvinyl alcohol (PVA). The PVA was then thermally decomposed at 850 °C, followed by sintering at approximately 1400 °C for 3 hours. The resulting samples were coated with silver paste to form electrodes. Finally, the samples were poled under a direct current field of approximately 30 kV/cm for 30 minutes.

### Structure characterizations

The XRD patterns were gained by X-ray diffraction (XRD) machine with Cu  $k_\alpha$  radiation (Bruker D8 Advanced XRD, Bruker AXS Inc., Madison, WI). Raman spectra were conducted by a Horiba Aramis Raman spectrometer (Horiba Scientific) with excitation sources of 532 nm. X-ray photoelectron spectroscopy (XPS) was obtained by X-ray photoelectron microprobe (XPS, K-Alpha+, Thermo Fisher Scientific, USA). The element distribution was analyzed by an electron probe microanalyzer (EPMA, JEOL JXA-8530F) with a wavelength dispersive spectrometer, and the probe size used is ~40–100 nm. Piezoresponse force microscopy (PFM) was conducted by a commercial microscope (MFP-3D, Asylum Research, Goleta, CA), applied to a conductive Pt-Ir-coated cantilever PPP-NCHPt (Nanosensors, Switzerland) with a bias voltage of 1 V. The local piezoresponse loops were obtained by the switching spectroscopy PFM mode with a triangular-wave voltage of 10 V. The electron-transparency sample for transmission electron microscopy (TEM) measurement was obtained by argon-ion beam milling system (Gatan PIPS 695, Gatan Inc., USA) under 0.1–6 kV. Then, the TEM measurement was conducted by a high-resolution TEM microscope (2100 F, JEOL, Japan) under 200 kV. The ceramic surface morphology was observed via a scanning electron microscopy (SEM) (JSM-6460LV, JEOL, Tokyo, Japan).

### Electrical properties measurements

The temperature-dependent dielectric properties at -60 – 150 °C were measured by an LCR analyzer (E4980A, Keysight, U.S.A.) at the frequency of 1, 10, and 100 kHz. The  $d_{33}$  was measured with a commercial Berlincourt-type  $d_{33}$  meter (ZJ-3A, China) for the poled samples. The ferroelectric hysteresis ( $P$ - $E$ ) loops and strain curves ( $S$ - $E$ ) were measured by a ferroelectric tester (aixACC TF Analyzer 2000 E, Germany) under a frequency of 1 Hz. Subcoercive measurements of the dielectric permittivity on unpoled samples were carried out via an impedance analyzer (Alpha-Analyzer, Novocontrol, Germany) interfaced with a high-voltage unit (HVB 300, Novocontrol, Germany). The complex impedance spectra were measured by a Novocontrol alpha-A impedance analyzer (Novocontrol Technologies GmbH & Co. KG, Montabaur, Germany) from 1 Hz to 3 MHz in the temperature range of 260–350 °C.

## DFT calculation

The bulk structures of  $\text{Ba}(\text{Ti}_{1-x}, \text{Sn}_x)\text{O}_3$  including the  $\text{BaTiO}_3$ ,  $\text{Ba}(\text{Ti}_{0.875}, \text{Sn}_{0.125})\text{O}_3$ ,  $\text{Ba}(\text{Ti}_{0.75}, \text{Sn}_{0.25})\text{O}_3$ , and  $\text{BaSnO}_3$  with cubic and tetragonal phases were studied by the first-principles density functional theory (DFT) calculations. The generalized gradient approximation (GGA) with the Perdew-Burke-Ernzerhofer (PBE) exchange-correlation function was employed in the calculations by using the Vienna Ab initio Simulation Package (VASP) with energy cutoff 500 eV<sup>47–50</sup>. The convergence criterion of energy and Hellmann-Feynman force is set at  $10^{-5}$  eV and  $10^{-3}$  eV/Å. The k-points mesh for single-cell structures ( $\text{BaTiO}_3$  and  $\text{BaSnO}_3$ ) is  $13*13*13$ , while k-points mesh in the remaining supercell structures ( $\text{Ba}(\text{Ti}_{0.875}, \text{Sn}_{0.125})\text{O}_3$  and  $\text{Ba}(\text{Ti}_{0.75}, \text{Sn}_{0.25})\text{O}_3$ ) is  $6*6*6$ . The  $\Gamma_4$  mode analysis is achieved with the support of ISODISTORT developed by Brigham Young University<sup>51,52</sup>. The visualization of calculation results is presented by VESTA<sup>53</sup> (See Fig. S9) and Paraview<sup>54</sup> (See Fig. S10). The Born Effective Charge (BEC) is calculated by using density functional perturbation theory (DFPT). The calculation of the Bader charge is implemented based on Bader Charge Analysis code<sup>55</sup>.

## Data availability

The source data generated in this study are provided in the Source Data file. More relevant data sets generated during and/or analyzed during the current study are available from the first authors and corresponding authors on reasonable request. Source data are provided with this paper.

## References

- Jaffe, B., Cook, W. R. & Jaffe, H. *Piezoelectric ceramics*. (Academic Press, London, 1971).
- Zhang, S. J. et al. Advantages and challenges of relaxor- $\text{PbTiO}_3$  ferroelectric crystals for electroacoustic transducers—A review. *Prog. Mater. Sci.* **68**, 1–66 (2015).
- Zheng, T., Wu, J., Xiao, D. & Zhu, J. Recent development in lead free perovskite piezoelectric bulk materials. *Prog. Mater. Sci.* **98**, 552–624 (2018).
- Shrout, T. R. & Zhang, S. J. Lead-free piezoelectric ceramics: Alternatives for PZT? *J. Electroceram.* **19**, 113–126 (2007).
- Rödel, J. & Li, J. F. Lead-free piezoceramics: status and perspectives. *MRS. Bull.* **43**, 576–580 (2018).
- Hong, C. H. et al. Lead-free piezoceramics—where to move on? *J. Materomics* **2**, 1–24 (2016).
- Hao, J. G., Li, W., Zhai, J. & Chen, H. Progress in high-strain perovskite piezoelectric ceramics. *Mater. Sci. Eng. Rep.* **135**, 1–57 (2019).
- Jo, W. et al. Giant electric-field-induced strains in lead-free ceramics for actuator applications - status and perspective. *J. Electroceram.* **29**, 71–93 (2012).
- Acosta, M. et al.  $\text{BaTiO}_3$ -based piezoelectrics: fundamentals, current status, and perspectives. *Appl. Phys. Rev.* **4**, 041305 (2017).
- Liu, W. F. & Ren, X. B. Large piezoelectric effect in Pb-free ceramics. *Phys. Rev. Lett.* **103**, 257602 (2009).
- Bell, A. J. & Deubzer, O. Lead-free piezoelectrics—the environmental and regulatory issues. *MRS Bull.* **43**, 581–587 (2018).
- Zhao, C., Huang, Y. & Wu, J. Multifunctional barium titanate ceramics via chemical modification tuning phase structure. *InfoMat.* **2**, 1163–1190 (2020).
- Gao, J. et al. Enhancing dielectric permittivity for energy-storage devices through tricritical phenomenon. *Sci. Rep.* **7**, 40916 (2017).
- Shi, T., Xie, L., Gu, L. & Zhu, J. Why Sn doping significantly enhances the dielectric properties of  $\text{Ba}(\text{Ti}_{1-x}\text{Sn}_x)\text{O}_3$ . *Sci. Rep.* **5**, 8606 (2015).
- Kalyani, A. K., Brajesh, K., Senyshyn, A. & Ranjan, R. Orthorhombic-tetragonal phase coexistence and enhanced piezo-response at room temperature in Zr, Sn, and Hf modified  $\text{BaTiO}_3$ . *Appl. Phys. Lett.* **104**, 252906 (2014).
- Gao, J. et al. Understanding the mechanism of large dielectric response in Pb-free  $(1-x)\text{Ba}(\text{Zr}_{0.2}\text{Ti}_{0.8})\text{O}_3\text{-}x(\text{Ba}_{0.7}\text{Ca}_{0.3})\text{TiO}_3$  ferroelectric ceramics. *Acta Mater.* **125**, 177–186 (2017).
- Lei, C., Bokov, A. A. & Ye, Z. G. Ferroelectric to relaxor crossover and dielectric phase diagram in the  $\text{BaTiO}_3\text{-BaSnO}_3$  system. *J. Appl. Phys.* **101**, 084105 (2007).
- Zhao, C. et al. Practical high piezoelectricity in barium titanate ceramics utilizing multiphase convergence with broad structural flexibility. *J. Am. Chem. Soc.* **140**, 15252–15260 (2018).
- Chen, K. et al. Improve piezoelectricity in  $\text{BaTiO}_3$ -based ceramics with large electrostriction coefficient. *J. Mater. Sci: Mater. Electron.* **31**, 12292–12300 (2020).
- Chen, K. et al. Large piezoelectric performance in zirconium doped  $\text{Ba}_{0.86}\text{Sr}_{0.14}\text{TiO}_3$  lead-free ceramics through utilizing multiphase coexistence. *J. Mater. Sci: Mater. Electron.* **30**, 18336–18341 (2019).
- Zheng, H. et al. Synergic and competitive effect of A-site substitution on structure and electric property in  $\text{BaTiO}_3$ -based ceramics. *J. Alloys Compd.* **937**, 168352 (2023).
- Cohen, R. E. Origin of ferroelectricity in perovskite oxides. *Nature* **358**, 136–138 (1992).
- Goldschmidt, V. M. Die gesetze der krystallochemie. *Naturwissenschaften* **14**, 477–485 (1926).
- Wu, B. et al. Insights into the correlation between ionic characteristics and microstructure and multiferroic properties in KNN-based ceramics with  $\text{BiMO}_3$  modification. *J. Alloys Compd.* **966**, 171568 (2023).
- Pan, W. et al. Defect chemistry of A site nonstoichiometry and the resulting dielectric behaviors in  $\text{Sr}_x\text{Ti}_{0.985}(\text{Nb}_{2/3}\text{Zn}_{1/3})_{0.015}\text{O}_3$  ceramics. *J. Am. Ceram. Soc.* **103**, 6298–6307 (2020).
- Horchidan, N. et al. Multiscale study of ferroelectric-relaxor crossover in  $\text{BaSn}_x\text{Ti}_{1-x}\text{O}_3$  ceramics. *J. Eur. Ceram. Soc.* **34**, 3661–3674 (2014).
- Slodczyk, A. & Colombari, P. Probing the nanodomain origin and phase transition mechanisms in (un)poled PMN-PT single crystals and textured ceramics. *Materials* **3**, 5007–5028 (2010).
- Veerapandiyan, V. K. et al. B-site vacancy induced Raman scattering in  $\text{BaTiO}_3$ -based ferroelectric ceramics. *J. Eur. Ceram. Soc.* **40**, 4684–4688 (2020).
- Tougaard, S. Practical guide to the use of backgrounds in quantitative XPS. *J. Vac. Sci. Technol. A* **39**, 011201 (2020).
- Shard, A. G. Practical guides for x-ray photoelectron spectroscopy: Quantitative XPS. *J. Vac. Sci. Technol. A* **38**, 041201 (2020).
- Tougaard, S. Formalism for quantitative surface analysis by electron spectroscopy. *J. Vac. Sci. Technol. A* **8**, 2197–2203 (1990).
- Zhang, K. et al. The self-compensation mechanism in barium titanate ceramics with colossal permittivity. *J. Alloys Compd.* **851**, 156856 (2021).
- Feng, Y. et al. Defects and Aliovalent Doping Engineering in Electroceramics. *Chem. Rev.* **120**, 1710–1787 (2020).
- Qiao, X. S. et al. Microstructure and electrical properties of non-stoichiometric  $0.94(\text{Na}_{0.5}\text{Bi}_{0.5+x})\text{TiO}_3\text{-}0.06\text{BaTiO}_3$  lead-free ceramics. *J. Am. Ceram. Soc.* **99**, 198–205 (2016).
- Wang, F. H. Evolution of microstructure and properties in BT-based lead-free magnetoelectric composite. *Ceram. Int.* **48**, 27472–27478 (2022).
- Wu, Y., Miao, J., Liu, Z. & Li, Y. Colossal permittivity and dielectric relaxations in  $\text{BaTi}_{0.99}(\text{Nb}_{0.5}\text{Ga}_{0.5})_{0.02}\text{O}_3$  ceramics. *Ceram. Int.* **41**, 846–850 (2015).
- Kang, B. S., Choi, S. K. & Park, C. H. Diffuse dielectric anomaly in perovskite-type ferroelectric oxides in the temperature range of 400–700 °C. *J. Appl. Phys.* **94**, 1904–1911 (2003).
- Wu, B. et al. Evolution of multilevel structures and electrical properties in potassium-sodium niobate-based lead free piezoceramics by anionic fluorine engineering. *J. Alloy. Compd.* **918**, 165604 (2022).

39. Balke, N., Lupascu, D. C., Granzow, T. & Rödel, J. Fatigue of lead zirconate titanate ceramics. i: unipolar and DC loading. *J. Am. Ceram. Soc.* **90**, 1081–1087 (2007).
40. Zhang, M. H. et al. Origin of high electromechanical properties in (K, Na)NbO<sub>3</sub>-based lead-free piezoelectrics modified with BaZrO<sub>3</sub>. *Phys. Rev. Mater.* **4**, 064407 (2020).
41. Wu, B. et al. Giant piezoelectricity and high Curie temperature in nanostructured alkali niobate lead-free piezoceramics through phase coexistence. *J. Am. Chem. Soc.* **138**, 15459–15464 (2016).
42. Zhang, M. H. et al. Deciphering the phase transition-induced ultra-high piezoresponse in (K, Na)NbO<sub>3</sub>-based piezoceramics. *Nat. Commun.* **13**, 3434 (2022).
43. Wu, B. et al. Contribution of irreversible non-180° domain to performance for multiphase coexisted potassium sodium niobate ceramics. *Nat. Commun.* **15**, 2408 (2024).
44. Lin, D. B. et al. Domain size engineering in tetragonal Pb(In<sub>1/2</sub>Nb<sub>1/2</sub>)O<sub>3</sub>–Pb(Mg<sub>1/3</sub>Nb<sub>2/3</sub>)O<sub>3</sub>–PbTiO<sub>3</sub> crystals. *J. Appl. Phys.* **110**, 084110 (2011).
45. Lu, N. & Zhu, J. Electron low energy-loss functions of Pb(Mg<sub>1/3</sub>Nb<sub>2/3</sub>)O<sub>3</sub>: Theory and experiment. *J. Appl. Phys.* **104**, 034109 (2008).
46. Choi, K. J. et al. Enhancement of ferroelectricity in strained BaTiO<sub>3</sub> thin films. *Science* **306**, 1005–1009 (2004).
47. Perdew, J. P., Burke, K. & Ernzerhof, M. Generalized gradient approximation made simple. *Phys. Rev. Lett.* **77**, 3865 (1996).
48. Kresse, G. Efficient iterative schemes for Ab initio total-energy calculations using a plane-wave basis set. *Phys. Rev. B* **54**, 11169 (1996).
49. Kresse, G. & Furthmüller, J. Efficiency of ab-initio total energy calculations for metals and semiconductors using a plane-wave basis set. *Comp. Mater. Sci.* **6**, 15–50 (1996).
50. Kresse, G. & Hafner, J. Ab initio molecular dynamics for liquid metals. *Phys. Rev. B* **47**, 558 (1993).
51. Campbell, B. J., Stokes, H. T., Tanner, D. E. & Hatch, D. M. ISODISPLACE: a web-based tool for exploring structural distortions. *J. Appl. Crystallogr.* **39**, 607 (2006).
52. Stokes, H. T., Orden, S. V. & Campbell, B. J. ISOSUBGROUP: an internet tool for generating isotropy subgroups of crystallographic space groups. *J. Appl. Crystallogr.* **49**, 1849 (2016).
53. Momma, K. & Izumi, F. VESTA 3 for three-dimensional visualization of crystal, volumetric and morphology data. *J. Appl. Crystallogr.* **44**, 1272 (2011).
54. Ayachit U. *The paraview guide: a parallel visualization application*. Kitware, Inc. (2015).
55. Yu, M. & Trinkle, D. R. Accurate and efficient algorithm for Bader charge integration. *J. Chem. Phys.* **134**, 064111 (2011).

## Acknowledgements

K. Wang acknowledges the support of the National Nature Science Foundation of China (Nos. 52325204, 52032005). H. -C. Thong acknowledges the support of Beijing Natural Science Foundation-International Scientists Project (No. IS24026). H. Tao acknowledges the support of the National Natural Science Foundation of China (No. 52202149), the Foundation of Sichuan Province Science and Technology Support Program (No. 2023NSFSC0968), and the Fundamental

Research Funds for the Central Universities, Southwest Minzu University (No. ZYN2023110). C. Zhao acknowledges the support of the National Natural Science Foundation of China (No. 12104093). B. Han acknowledges the support of the National Natural Science Foundation of China (No. 51972005, U21A2055).

## Author contributions

B.W., C.Z., F.Z.Y., and B.H. conceived the idea of this work. H.Z. and H.T. prepared the ceramics. Z.X. and Y.X.L. performed the electrical and structural measurements and analyzed the data with the guidance by J.M. and K.W.Y. Q.W. and H.C.T. performed the DFT Calculation. H.T., C.Z., B.H., and K.W. provided financial and technical support for this work. Z.H., Z.X., C.F.W., and N.L. help to revise the paper.

## Competing interests

The authors declare no competing interests.

## Additional information

**Supplementary information** The online version contains supplementary material available at <https://doi.org/10.1038/s41467-024-52031-z>.

**Correspondence** and requests for materials should be addressed to Chunlin Zhao, Fang-Zhou Yao or Bing Han.

**Peer review information** *Nature Communications* thanks Hua Hao and the other anonymous reviewer(s) for their contribution to the peer review of this work. A peer review file is available.

**Reprints and permissions information** is available at <http://www.nature.com/reprints>

**Publisher's note** Springer Nature remains neutral with regard to jurisdictional claims in published maps and institutional affiliations.

**Open Access** This article is licensed under a Creative Commons Attribution-NonCommercial-NoDerivatives 4.0 International License, which permits any non-commercial use, sharing, distribution and reproduction in any medium or format, as long as you give appropriate credit to the original author(s) and the source, provide a link to the Creative Commons licence, and indicate if you modified the licensed material. You do not have permission under this licence to share adapted material derived from this article or parts of it. The images or other third party material in this article are included in the article's Creative Commons licence, unless indicated otherwise in a credit line to the material. If material is not included in the article's Creative Commons licence and your intended use is not permitted by statutory regulation or exceeds the permitted use, you will need to obtain permission directly from the copyright holder. To view a copy of this licence, visit <http://creativecommons.org/licenses/by-nc-nd/4.0/>.

© The Author(s) 2024